A High-Power Terahertz Source Over 10 mW at 0.45 THz Using an Active Antenna Array With Integrated Patch Antennas and Resonant-Tunneling Diodes

Yasushi Koyama, *Member, IEEE*, Yuki Kitazawa, Koji Yukimasa, Tatsuro Uchida, Takeshi Yoshioka, Kokichi Fujimoto, Takahiro Sato, Jun Iba, Katsuhito Sakurai, and Takeshi Ichikawa

***Abstract*—We propose a compact, high-power, and high-directivity surface-emitting terahertz (THz) source based on an array of active antennas with integrated patch antennas and resonant-tunneling diodes (RTDs). An array configuration of active antennas, each with an integrated patch antenna and two RTDs and coupled by microstrip lines, enables spatial power combining and improves directivity through coherent oscillation. We confirmed a maximum radiation power of 11.8 mW in a prototype 6 × 6 array at an oscillation frequency of 0.45 THz. Parasitic oscillation at low frequencies was suppressed by use of a bias stabilization circuit consisting of series-connected resistors and capacitors, and the dc to RF efficiency of this device was estimated to be approximately 1%. The radiant intensity of 210 mW/sr and the 3-dB beamwidth of 13° for the measured 6 × 6 array confirmed that directivity was improved by coherent oscillation based on mutual injection locking. The directivity of the patch antenna capable of surface emission can be controlled only by the number of antennas, even if there is no secondary radiator, such as an Si lens. The obtained results suggest that RTDs are promising as practical THz sources for realizing applications of THz imaging and 6G communication.**

***Index Terms*—Active antenna array, patch antenna, resonant tunneling diode (RTD), terahertz (THz) oscillator.**

I. INTRODUCTION

THE terahertz (THz) frequency band is attracting attention for applications in security body scanner, nondestructive inspection, and 6G communication. One of the key components for such applications is a compact, high-power semiconductor THz source [1]–[3]. In recent years, there has been much technology development: quantum cascade lasers have been proposed in the field of optical devices, and THz oscillators based on Si, Si-Ge, and In-P transistors in the field of electronic devices [4]–[9]. Resonant-tunneling diodes (RTDs), which offer the advantage of being capable of fundamental oscillation in high-frequency bands, including THz, are also candidates for efficient semiconductor THz sources operating at room temperature [10]–[16].

High-frequency oscillation of 1.98 THz and high-power radiation of 0.61 mW at 0.55 THz have been reported in a single active antenna with integrated slot antenna and an In-P based RTD [10]. One of the important challenges for THz sources is to ensure a high output of radiation power, and technologies to combine the power of active antennas by using array configurations have been proposed [6], [11], [12], [17]–[19]. For example, in an array of two active antennas with integrated slot antennas and RTDs, an oscillation of 0.6 mW at 0.62 THz by coherent power combination based on mutual injection-locking has been reported [11]. Recently, a radiation power of 0.73 mW at 1.0 THz has been obtained by incoherent power combination in an array configuration of 89 active antennas [12]. According to previous research, strong coupling and a reduction of frequency variation of the active antennas constituting the array are required to achieve coherent power combination based on stable injection locking.

Meanwhile, patch antennas are often used in the field of millimeter waves as a means of beamforming by an array configuration, and they work well with microstrip lines, which are easy to fabricate with planar integration technology. For example, directivity control and quasi-optical power combining based on locking with strong coupling have been reported for looped arrays of four active antennas with integrated Gunn diodes and microstrip lines, which connect patch antennas [19]. We have previously reported THz oscillation of an active antenna with integrated RTD and patch antenna capable of surface emission [20], [21]. However, the obtained radiation power did not exceed 10 μW, and thus was deemed insufficient as a THz source for practical use in the applications mentioned earlier.

In this article, we propose a compact, high-power, and high-directivity THz source based on an array of active antennas with integrated patch antennas and RTDs. With a 6 × 6 matrix array configuration of active antennas, each with an integrated patch antenna and two RTDs, we obtained a radiation power of up to 11.8 mW at an oscillation frequency of 0.45 THz. By coupling the individual antennas in the 6 × 6 array using microstrip lines for mutual injection locking, we realized directivity control based on coherent oscillation and obtained a radiation intensity of 210 mW/sr and a 3-dB beamwidth of 13° without a lens.

This article is structured as follows. Section II provides an outline of an RTD-based THz source, and Section III describes

---

Manuscript received 31 January 2022; revised 10 May 2022; accepted 26 May 2022. Date of publication 8 June 2022; date of current version 3 September 2022. *(Corresponding author: Yasushi Koyama.)*

Yasushi Koyama, Yuki Kitazawa, Tatsuro Uchida, Takeshi Yoshioka, Kokichi Fujimoto, Takahiro Sato, Jun Iba, Katsuhito Sakurai, and Takeshi Ichikawa are with the Device Technology Development Headquarters, Canon, Inc., Tokyo 146-8501, Japan (e-mail: koyama.yasushi@mail.canon).

Koji Yukimasa is with the Digital Business Platform Development Headquarters, Canon, Inc., Tokyo 146-8501, Japan.

Color versions of one or more figures in this article are available at https://doi.org/10.1109/TTHZ.2022.3180492.

Digital Object Identifier 10.1109/TTHZ.2022.3180492

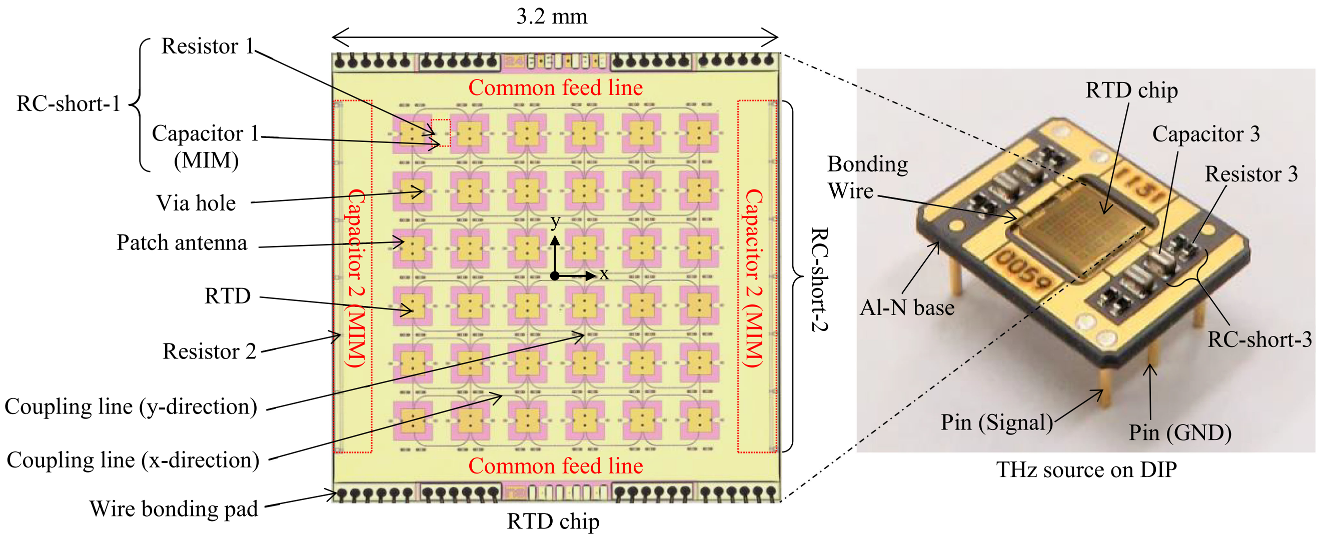

Fig. 1. Outline of RTD-based THz source (0.45 THz, 6 × 6 array).

a single active antenna with integrated patch antenna and two RTDs. Section IV describes the array design, and Section V discusses the characteristics of the prototyped THz sources. Finally, Section VI concludes this article.

II. OUTLINE OF RTD-BASED THZ SOURCE

Fig. 1 shows photographs of the prototyped THz source chip and other components. The RTD chip (3.2 × 3.2 mm^2) comprises 36 antennas, coupling lines, common feed line, and pads for wire bonding. The antennas are active antennas each of which is integrated with a square patch antenna of 170 × 170 μm^2 and two RTDs. The patch antennas have a structure in which two conductor layers, namely an upper patch electrode and a lower ground electrode, sandwich a 7 μm-thick dielectric layer that is made of benzocyclobutene (BCB) and silicon dioxide (SiO_2) and has two RTDs buried therein. An electrical connection between the RTDs and the two upper and lower electrodes using metal via provides bias power feeding to the diodes and the THz oscillation of the antenna [21].

The active antennas are designed to oscillate at 0.45 THz and are arranged in a 6 × 6 matrix at a pitch of 400 μm, which corresponds to 0.6 × λ_{osc}, where λ_{osc} is the wavelength of the oscillation frequency (f_{osc}) in a vacuum. The antennas are connected through coupling lines for transmitting THz waves, which extend in two directions (x and y), and the design is such that all antennas oscillate at the same phase by mutual injection locking. One antenna is connected to each of the two ends of a coupling line, which consists of a microstrip line with a characteristic impedance of 100 Ω, whose substrate is composed of SiO_2, BCB, and silicon nitride (SiN_x). The antennas and the coupling lines are connected by ac coupling through a metal-insulator–metal (MIM) capacitor of 10 fF, formed with SiN_x interposed in a portion where the patch electrode and the microstrip line overlap, at the radiation edge of the patch antenna. SiO_2, BCB, and SiN_x are stacked in order from the lower ground electrode side, and SiO_2 mainly has role as an insulator of a wiring layer for the common feed line, BCB as thick-film dielectric of the patch antenna, and SiN_x as a dielectric of MIM for ac coupling. To obtain an in-phase coherent oscillation, the electrical length of the coupling lines in the x and y directions is designed to be λ_g and $\lambda_g/2$, respectively. Here, λ_g is the guided wavelength of electromagnetic waves of f_{osc} inside the coupling lines.

To address an issue of the complicated wiring layout with an increase in the number of antennas, a bias voltage for RTDs is collectively supplied to all the antennas in the array using one common feed line. The common feed line for power supply is composed of a wiring layer located between the patch electrode and the ground electrode. A single antenna has two via holes located at a node of the electric field resonating at f_{osc}, and the via holes electrically connect the patch electrode and tapered wiring formed on the wiring layer. One antenna is connected through two tapered wirings to the common feed line, which is arranged in a grid between the antennas. An *RC* short (*RC*-short-1) is connected to the tapered wiring. In the *RC* short, a 10-Ω resistor (Resistor 1), and a 10-pF MIM capacitor (Capacitor 1) are series-connected, and thus parasitic oscillation originating from the wiring structure around the antennas is suppressed. Furthermore, parasitic oscillation of up to 3 GHz is suppressed by an electrical connection of *RC* shorts (*RC*-short-2) located on the right end and left end of the chip, to the common feed line. Here, each *RC*-short-2 is composed of seven parallel 7-Ω resistors (Resistors 2) and one 500-pF MIM capacitor (Capacitor 2), with each resistor and capacitor being series-connected. The RTD chip is mounted to a standard-pitch six-pin dual in-line package (DIP) having dimensions of 10 × 8 × 4 mm and using an aluminum-nitride (Al-N) base material to prevent thermal degradation. The DIP and the common feed line of the RTD chip are electrically connected via the bonding wires.

III. SINGLE ANTENNA WITH TWO RTDS

The RTD-integrated active antenna reported in this article uses double barrier RTDs based on In-Ga-As/In-Al-As fabricated by epitaxial growth on an In-P substrate. The IV curves acquired by

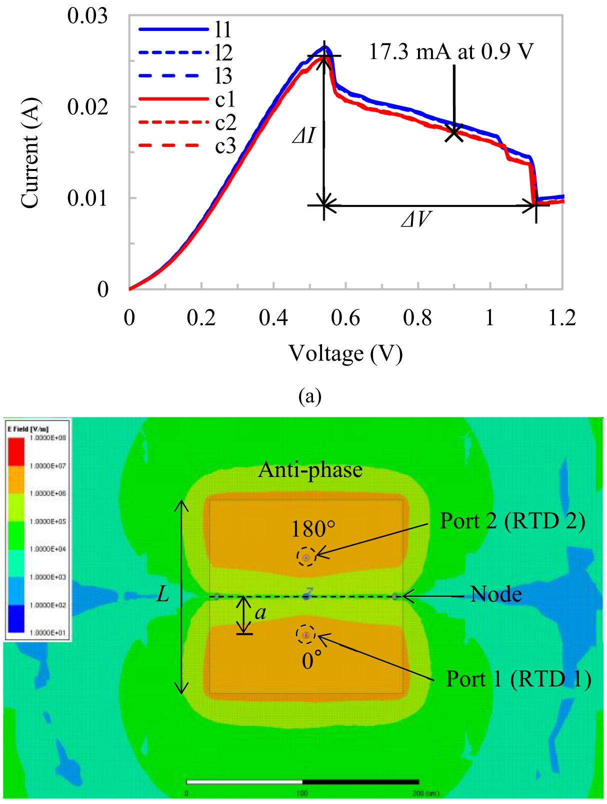

(a)

(b)

Fig. 2. (a) Measured IV curves of six RTDs. (b) Simulated E-field distribution in single antenna.

measurement of six RTDs are shown in Fig. 2(a). The IV curves show the plateau phenomenon that is typically observed in the negative differential resistance (NDR) region due to parasitic oscillation. The red and blue lines in Fig. 2(a) indicate the measurement results of three RTDs in one chip at the center of the wafer (c1 to c3), and at 20 mm away from the center (l1 to l3). The average and 3σ variation of the peak current were 25.4 and 0.2 mA for c1 to c3, 26.5 and 0.2 mA for l1 to l3, and 25.9 and 1.6 mA between two chips 20 mm apart. The parameters of RTD extracted from the IV curves (c1 to c3) were $\Delta I = 14$ mA, $\Delta V = 0.55$ V, and NDR $= -39\ \Omega$. The transient analysis explained later was carried out using an ac source model that shows the current–voltage characteristics of this measured IV curve as approximated by a cubic function. For all performance evaluations (power, frequency, and directivity), the bias voltage ($V_{\rm bias}$) applied to the RTDs is 0.9 V, and the current per RTD as read from the IV curve in Fig. 2(a) under this driving condition is 17.3 mA.

Fig. 2(b) shows the electric field distribution at an oscillation frequency of 0.45 THz localized inside the active antenna, simulated using the 3-D electromagnetic field simulator HFSS (ANSYS, Inc.). In the figure, L is the resonator length of the square patch antenna, which is expressed as $L = \lambda_{\rm osc}/2\varepsilon_r{}^2$, where ε_r is the effective relative permittivity of the dielectric layer consisting of BCB and $\mathrm{SiO_2}$. Offset is a parameter for adjusting the input impedance of the RTD connected to the antenna, and is expressed in terms of the position of the RTD in the antenna, for example, offset $= 100 \times a/L$, where a is the distance from the center of the patch antenna to the RTD.

The two RTDs are arranged in mirror symmetry with respect to the center of the patch antenna and operate in push–pull mode [16], [22]. During oscillation, a standing wave node of $f_{\rm osc}$ is formed in a direction perpendicular to a straight line passing through the center of the patch antenna and connecting the two RTDs. As a result, the two RTDs are forced to oscillate at the same frequency and in an anti-phase mode. As shown in Fig. 2(b), in the push–pull mode using two RTDs, the standing wave is symmetrical and the position of the node is fixed at the center of the antenna. On the other hand, in the case of one RTD, the position of the node is shifted in the direction of the RTD so that the symmetry of the standing wave is disturbed. Therefore, the push–pull mode is considered to contribute to the stabilization of the mutual coupling through the microstrip lines in the antenna array. It also has the advantages that the symmetry of the radiation pattern is improved, and the radiation power is doubled with two diodes in ideal.

The oscillation frequency ($f_{\rm osc}$) of the active antenna was estimated under the condition that the two RTDs oscillate by mutual injection locking in anti-phase, that is, the following two expressions are satisfied [17]:

$$\mathrm{Re}\left[Y_{\rm RTD} + Y_{11} - Y_{12}\right] \le 0 \tag{1}$$

$$\mathrm{Im}\left[Y_{\rm RTD} + Y_{11} - Y_{12}\right] = 0. \tag{2}$$

Here, $Y_{\rm RTD}$ is the admittance of one RTD; it has been calculated by using parameters extracted from the IV curve of Fig. 2(a) and parameters attributed to the semiconductor structure set out in [20] and [21], from the equivalent circuit of Asada *et al.*'s work [23]. Port 1 (RTD 1) and port 2 (RTD 2) in the figure are input ports for connecting the two RTDs to the antenna, and Y_{11} and Y_{12} are, respectively, the admittance of port 1 and the mutual admittance between ports 1 and 2, and both are calculated by using HFSS.

Fig. 3(a) shows the simulated admittance of an active antenna designed with $L = 170\ \mu$m and offset $= 20\%$. The oscillation frequency ($f_{\rm osc}$) is mainly determined by the reactance (Im $[Y_{11} - Y_{12}]$) of the patch antenna and the diode capacitance (C_d) of the RTD, with C_d estimated to be 10 fF based on a comparison between the measured oscillation frequency and the simulation. Fig. 3(b) shows the correlation between $f_{\rm osc}$ and the antenna structure (L and offset), with the dots and the lines, respectively, representing the measurement and simulation results. The radiation power and the frequency were measured by using a TK Terahertz Absolute Power Meter System (Thomas Keating, Ltd.) and Fourier-transform-infrared (FTIR) spectroscopy (JASCO Faris-1), respectively. The prototype device oscillates at a frequency of 0.44–0.54 THz, and the correlation with L and offset shows adequate agreement between the measurements and simulations.

The radiation power is estimated from the equation of $P_{\rm out}$ described in [9], using ΔI, ΔV, Re $[Y_{11} - Y_{12}]$, and the radiation efficiency (29%) of the antenna calculated by HFSS. In the power estimation of the push–pull mode, $G_{\rm ANT}$ is considered as Re

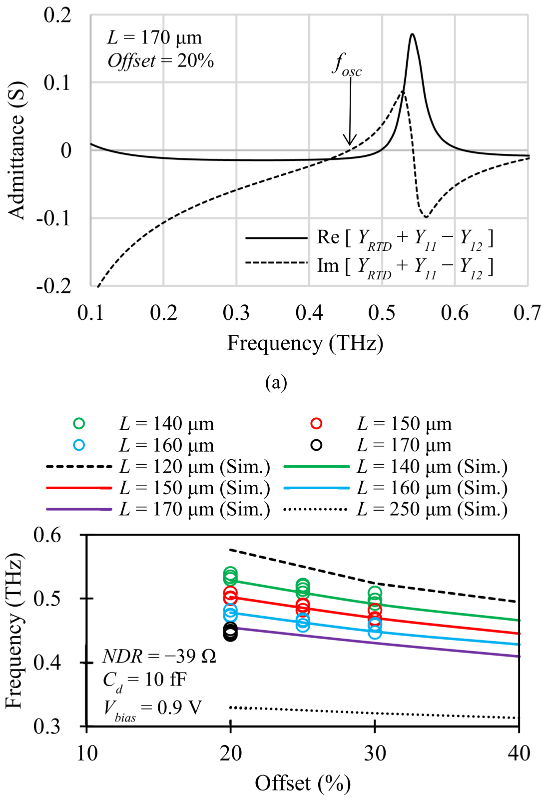

(a)

(b)

Fig. 3. (a) Calculated admittance of single antenna. (b) Correlation between oscillation frequencies and antenna structures.

$[Y_{11} - Y_{12}]$, $G_{\rm rad}$ as 0.29 × Re $[Y_{11} - Y_{12}]$, and $G_{\rm RTD}$ as $3\,/\,2 \times \Delta I\,/\,\Delta V$, and the power is calculated as double of $P_{\rm out}$ since two RTDs are used. Here, $G_{\rm ANT}$ is the conductance of the antenna, $G_{\rm rad}$ is the radiation conductance, and $G_{\rm RTD}$ is the negative differential conductance of RTD [10]. The estimated power of the device shown in Fig. 3(a) was 0.38 mW and was confirmed to roughly match the measurement results of the power meter. There is a difference between the measured and calculated results, and it is considered that the power is not simply double of one RTD, due to the factors, such as the asymmetry resulting from the variations in fabrication, and the loss of the via connecting the antenna to the RTD. With an offset in the range below 20%, the input impedance of the antenna is low and the locking in push–pull mode becomes unstable, and so it is preferable that the offset is at least 20%. These results verified that it is possible to control the frequency of the active antenna with integrated patch antenna and two RTDs by structural adjustments and $f_{\rm osc}$ is tunable up to 0.6 THz by changing the design.

IV. DESIGN OF ARRAY CONFIGURATION

A. Design of Active Antenna Array

Technologies to enable spatial power-combining through coherent oscillation by arranging active antennas in an array and mutually injection locking the individual antennas have been reported in previous research, both from theoretical and experimental aspects [6], [11], [12], [17]–[19]. The array of active antennas with integrated patch antennas and RTDs proposed in this article is also designed on the basis of the concepts of previous research. As the single active antennas constituting the array, we used antennas ($L = 170\ \mu$m, offset $=$ 20%) that were designed for $f_{\rm osc}$ of 0.45 THz, as described in Section III, and, the individual antennas were arranged at a pitch of 0.6 × $\lambda_{\rm osc}$ in order to avoid the generation of grating lobes.

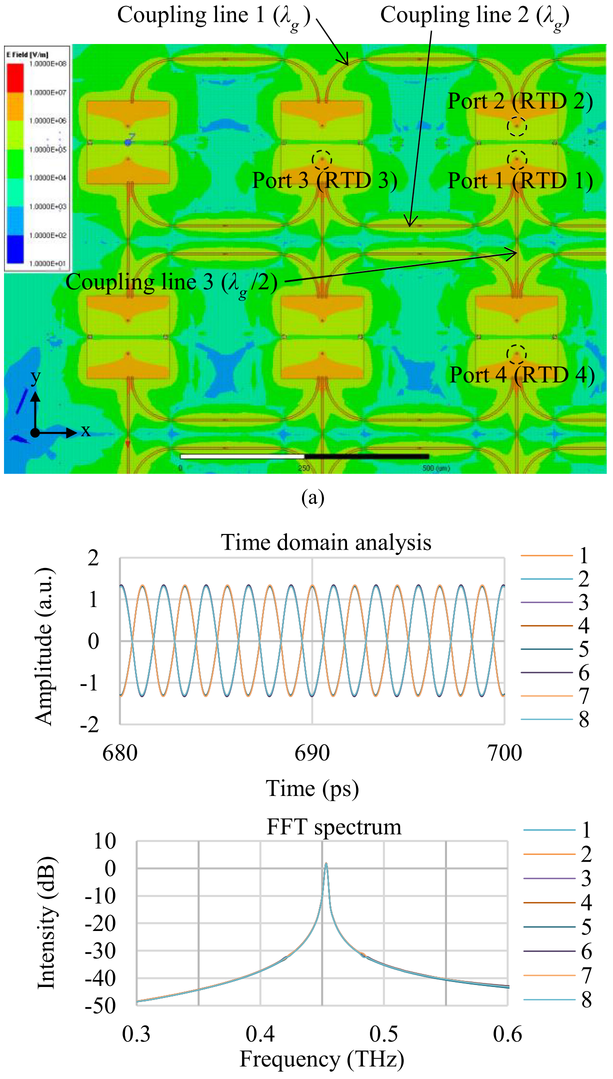

(a)

(b)

Fig. 4. (a) Simulated E-field distribution in 4 × 4 array. (b) Transient analysis results of 2 × 2 array.

Fig. 4(a) shows the simulation result of an electric field distribution in an in-phase mode of a 4 × 4 array at 0.45 THz using the finite array approximation of HFSS. In order to align the phases of the individual antennas, the antennas are coupled by coupling lines based on microstrip lines extending in the *x*-direction (perpendicular to the resonance direction of the patch antenna) and the *y*-direction (parallel to the resonance direction of the patch antenna). The coupling of the two directions *x* and *y* reduces the unbalance of locking between antennas into one direction and realizes a stronger radiant intensity and sharper directivity through uniform power combination. The electrical length of the coupling lines is suitably designed so that the phases between adjacent antennas are fixed in phase. Three types of coupling lines are used to connect the antennas with each other: coupling line 1 and coupling line 2 (a structure obtained by mirroring coupling line 1 in the *y*-direction) of electrical length λ_g, which provide coupling in the *x*-direction, and coupling line 3 of electrical length $\lambda_g/2$, which provides coupling in the *y*-direction. To make adjacent antennas oscillate at the same frequency and phase with in-phase mutual injection locking, the structure of each coupling line is designed, approximately, to satisfy all of the following expressions:

$$\mathrm{Re}\left[Y_{\mathrm{RTD}} + Y_{11} + Y_{13}\right] \leq 0 \tag{3}$$

$$\mathrm{Im}\left[Y_{\mathrm{RTD}} + Y_{11} + Y_{13}\right] = 0 \tag{4}$$

$$\mathrm{Re}\left[Y_{\mathrm{RTD}} + Y_{11} + Y_{14}\right] \leq 0 \tag{5}$$

$$\mathrm{Im}\left[Y_{\mathrm{RTD}} + Y_{11} + Y_{14}\right] = 0. \tag{6}$$

Here, Y_{13} is the mutual admittance between port 1 and port 3, and Y_{14} is the mutual admittance between port 1 and port 4 in Fig. 4(a). In addition, a single active antenna is designed to satisfy the anti-phase locking conditions (1) and (2), as described in Section III.

The unit antenna serving as the basis for the array design has a total of six coupling lines, two each of coupling lines 1 to 3 per antenna. Three of these coupling lines are connected to the upper radiation edge of the square patch antenna and three to the lower radiation edge and a pair of adjacent antennas is connected to the two ends of one coupling line. In order to suppress multimode oscillation, the coupling lines of the antennas placed at the edges of the array, which have no neighboring antennas to connect, were removed to form a loop array without any ends. The antennas and coupling lines are connected by ac coupling through a 10-fF MIM capacitor to form an electrical short circuit in the THz frequency band and an electrical open circuit in the lower frequency band below 10 GHz between the individual antennas. Using this symmetrical structure of the unit antenna, the array design can be simplified and the number of antennas can be increased. Furthermore, the symmetrical topology contributes to the uniformity of the radiating pattern of the antenna array. Fig. 4(b) shows the results of an oscillation simulation using a transient analysis by HFSS of a 2 × 2 array designed according to the aforementioned rules. From the time waveforms of the voltage amplitudes of all eight ports, the oscillations of anti-phase within the antenna and in-phase between the antennas are confirmed with a fundamental oscillation frequency of 0.45 THz. The allowable variations of amplitude, phase, and frequency between antennas to maintain mutual injection locking in 2 × 2 array are estimated to be 18%, 9%, and 1.5%, respectively. In this study, the coupling lines designed using the above 2 × 2 array are extended up to 6 × 6 active antenna array by periodically arranging them.

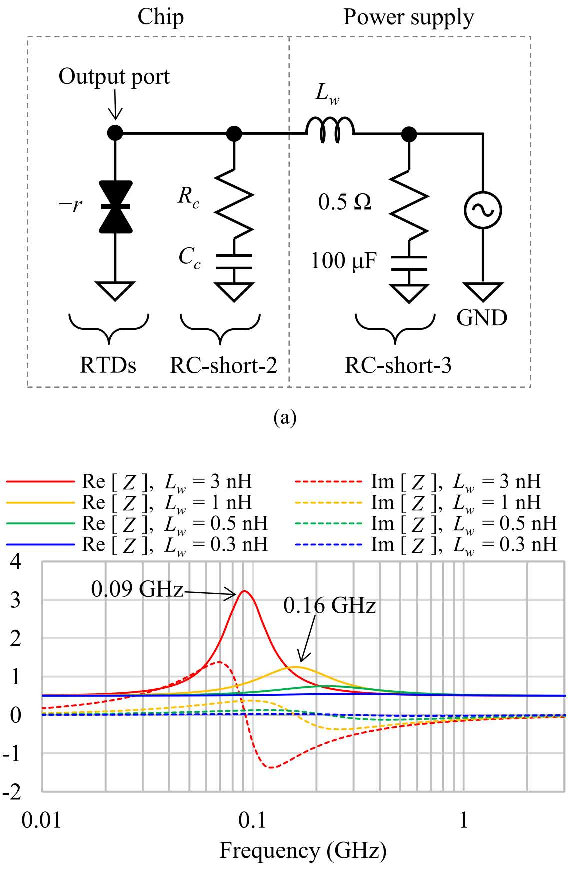

Fig. 5. (a) Circuit diagram of bias stabilizer for array configuration. (b) Results of impedance *Z* analysis ($r = 0.55\ \Omega$, $R_c = 0.5\ \Omega$, $C_c = 1$ nF).

B. Design of Bias Stabilizer

Shunt resistors, which are commonly used for suppressing parasitic oscillation, require a dc short circuit with a resistance approximately equivalent to the absolute value of the NDR, and, for this reason, the dc power consumption of the device is almost doubled [15]. Meanwhile, in an array configuration of active antennas with integrated antennas and RTDs, the absolute value of the NDR in the oscillation circuits is typically less than 1 Ω because, when the number of antennas increases, the number of RTDs also increases. Therefore, using a conventional method of suppressing parasitic oscillation for the array would lead to an increase in the maximum rating of the power supply and degrade the reliability due to the heat generated by the shunt resistors. The array antenna reported in this article addresses this issue by using capacitive impedance ($1/\omega C$, ω: angular frequency, C: capacitance) to provide an *RC* short circuit with a series connection of resistors and capacitances [15], [24].

Fig. 5(a) shows the circuit diagram of the bias stabilization circuit in the low-frequency band (typically 3 GHz or lower), which is used to design *RC* shorts placed on the chip edge and the DIP. In Fig. 5(a), $-r$ is the NDR combined for all RTDs connected in parallel in the array and r will be 0.55 Ω in a 6 × 6 array with 72 RTDs. Here, the impedance of the antennas, the common feed line, and the *RC*-short-1, which is used to stabilize a single active antenna up to several tens of gigahertz, are ignored because of low capacitance and low inductance. In a simplified estimate, the characteristic impedance of the two *RC* shorts (*RC*-shorts-2 and -3) connected in parallel with *r* should be less than or equal to *r*, respectively, to suppress parasitic oscillation at low frequencies. For example, *RC*-short-3 is the combined resistance and capacitance of the *RC* shorts, which are surface-mounted on the DIP shown in Fig. 1. In Fig. 5(a), *RC*-short-3 is expressed as a snubber circuit with a 100-μF bypass capacitor and is designed so that the wiring impedance of the power supply circuit is less than 0.55 Ω at 5 kHz or higher.

R_c and C_c in the circuit are the combined resistance and capacitance of the two *RC*-short-2 placed at the RTD chip edge, with R_c and C_c being 0.5 Ω and 1 nF, respectively. At frequencies of 10 MHz and above, where the inductive impedance (ωL, L: inductance) cannot be ignored, the parasitic inductance (L_w) between *RC*-short-2 and -3, which mainly caused by the inductance of the bonding wire and the feed line in the DIP, needs to be reduced to 1 nH or less in order to keep the characteristic impedance lower than 1 Ω at the output port in Fig. 5(a). L_w is estimated by modeling the structure from the wire bonding pad at the chip edge to the *RC*-shunt-3 on the DIP using HFSS. In the device reported here, L_w has been reduced to 0.3 nH or lower by increasing the number of bonding wires, and arranging four sets of feed lines and *RC* short circuits in parallel in the DIP. Fig. 5(b) shows the impedance at the output port in Fig. 5(a), which was calculated by an ac analysis of SPICE. The calculation results show that, under the condition where L_w is 1 nH or higher (L_w = 1 or 3 nH), parasitic oscillation of around 0.1 GHz occurs due to the *LC* resonance of L_w and C_c. In contrast, the *LC* resonance tends to be suppressed where L_w is 0.5 nH or less, and where L_w is 0.3 nH, no parasitic oscillation at 0.01 to 3 GHz occurs up to 6 × 6 array since the real part of impedance is 0.55 Ω. To realize an antenna array over 6 × 6 with the present RTD, it is necessary to further reduce L_w or increase C_c to suppress the parasitic oscillations, and in addition to the circuit in Fig. 5(a), a concrete design of the whole stabilization circuit is required, taking into account the antenna array, the feed line and the *RC* shorts in the chip. *RC* shorts using capacitive impedance make it possible to realize an active antenna array operates in the THz band while suppressing parasitic oscillation, dc power consumption, and thermal degradation of the devices.

V. EXPERIMENTAL RESULTS OF THZ SOURCE WITH ARRAY CONFIGURATION

Fig. 6(a) shows the correlation between the number of antennas and the radiation power measured using a TK power meter at $V_{\text{bias}} = 0.9$ V in the prototype antenna arrays (2 × 2, 4 × 4, 5 × 5, and 6 × 6). The measured radiation power increases linearly with the number of antennas, and the radiation power per single antenna calculated from the slope of the linear approximation is 0.32 mW, which is in agreement with the results for the single antenna. The maximum radiation power from the 6 × 6 array consisting of 36 antennas is 11.8 mW, and f_{osc} is 0.446 THz shown in Fig. 6(b). The oscillation frequency measured for the 112 prototype RTD chips of 6 × 6 array design was 0.449 THz on average, with a 3σ variation of 0.008 THz. In the spectrum shown in Fig. 6(b), only a single peak of the fundamental oscillation frequency is observed, indicating that there is no peak separation, multimode oscillation, or satellite in the range of 0.1 to 0.8 THz. Furthermore, the same results have been obtained for the measured oscillation frequencies of arrays with fewer antennas (2 × 2, 4 × 4, and 5 × 5), which are consistent with those of the single active antenna. According to the aforementioned results, it is assured that the coherent oscillations of all active antennas in the array are realized as a result of the mutual injection locking at 0.45 THz. As mentioned

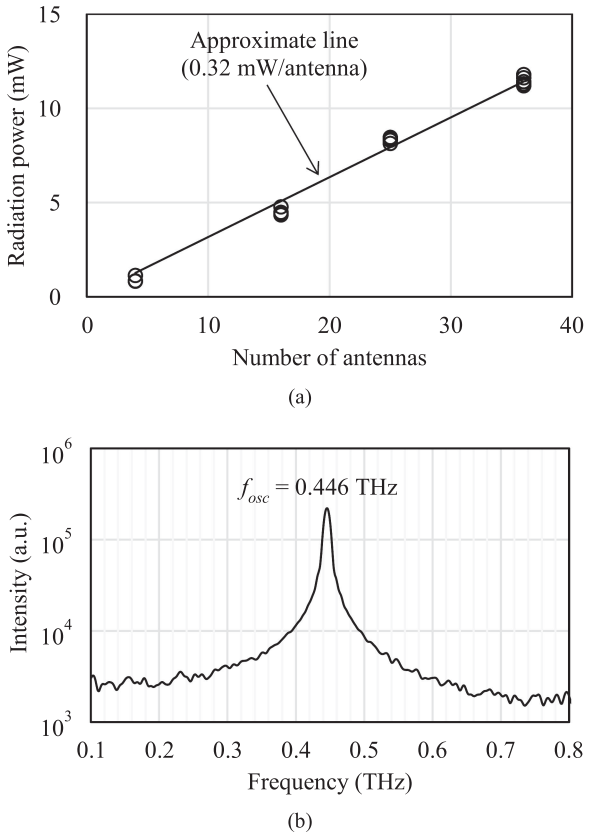

Fig. 6. Measured (a) radiation power as a function of antenna number in the antenna arrays and (b) FTIR spectrum for a 6 × 6 array at $V_{\text{bias}} = 0.9$ V.

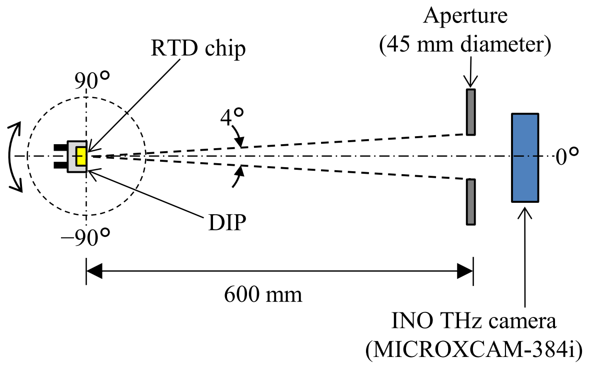

Fig. 7. Schematic diagram of directivity measurement system.

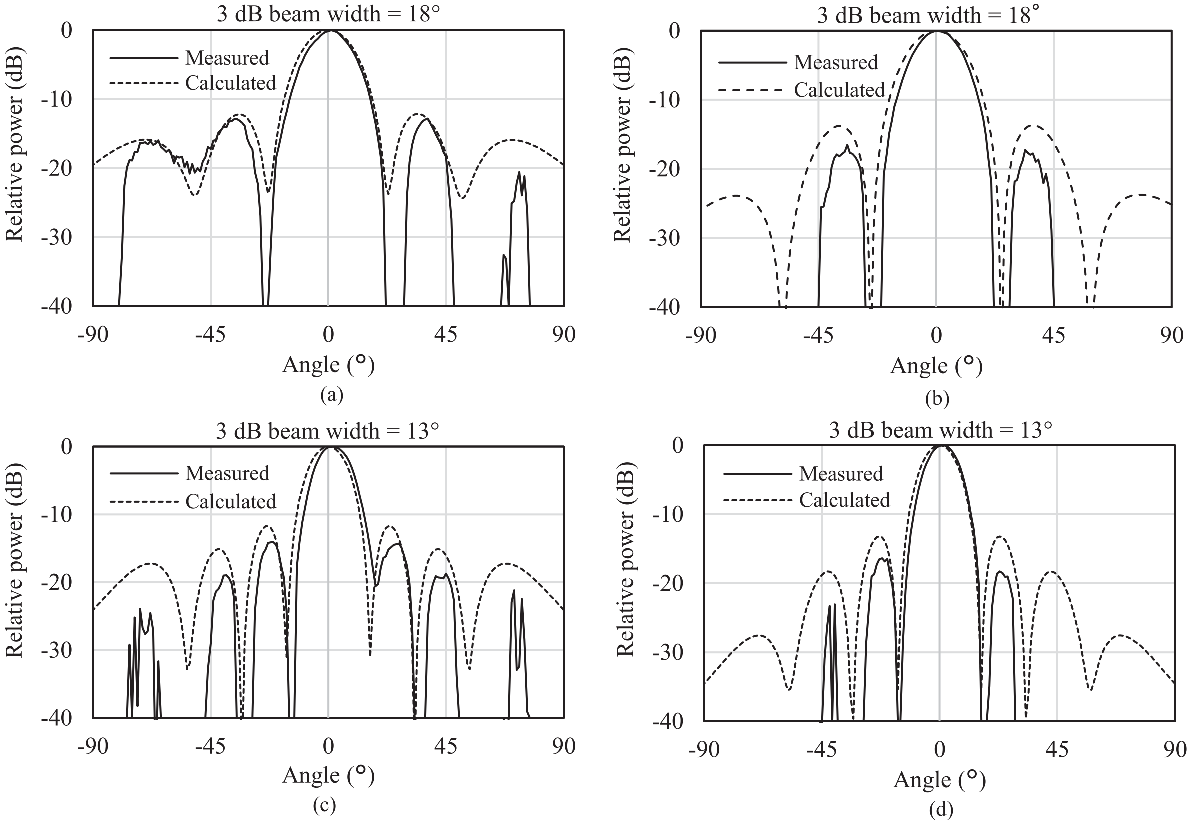

Fig. 8. Measured radiation patterns of active antenna array: (a) E-plane of 4 × 4 array, (b) H-plane of 4 × 4 array, (c) E-plane of 6 × 6 array, and (d) H-plane of 6 × 6 array.

in Section III, the current and voltage per RTD under driving conditions are 17.3 mA and 0.9 V, respectively. Therefore, the dc power consumption of a 6 × 6 array containing 72 RTDs results in 1.12 W, and the dc to RF efficiency is estimated to be about 1%.

Fig. 7 shows a schematic diagram of the simplified measurement system to evaluate the directivity and radiation pattern of the antenna array. The RTD chip mounted on the DIP radiates THz waves from the antenna array in the vertical upward direction (3 o'clock direction in Fig. 7) with respect to the chip surface. The directivity was evaluated by measuring the power incident on a bolometer camera (INO MICROXCAM-384i) placed behind an aperture (45-mm diameter) 600 mm away from the RTD chip surface [25]. The radiating pattern measurement and evaluation were performed by rotating the RTD chip at a 1° pitch from $-90°$ to $+90°$ around a rotation axis perpendicular to the sheet and through the center of the chip surface. From the geometric configuration shown in Fig. 7, the angular resolution and solid angle of the setup are estimated to be 4° and 0.0044 sr, respectively.

In an active antenna array with stable in-phase oscillation, the power (i.e., radiant intensity) per unit solid angle radiated vertically upward from the antenna is enhanced by the sharpening of the directivity and the radiant intensity ideally increases in proportion to the square of the number of antennas [17], [19]. Fig. 8 shows the radiating patterns of two types of array antennas, 4 × 4 and 6 × 6, measured in the electric field plane (E-plane) and the magnetic field plane (H-plane). Here, the solid lines represent measurements, and the dashed lines indicate simulation results of HFSS using the finite array approximation. For both the E-plane and the H-plane, the 3-dB beamwidth of the main lobe is 18° for 4 × 4 and 13° for 6 × 6, and directivity sharpening by arraying can be confirmed from the aspects of both measurement and simulation. The maximum sidelobe level was -13 dB, and the same number of lobes as in the simulation was observed. Since the antenna array was designed with a pitch of $0.6 \times \lambda_{\mathrm{osc}}$, no grating lobes were observed within the range of ±90°. The slight difference between the measured and simulated results is probably caused by the insufficient accuracy of the directivity measurement setup used in this study. The improvement for acquiring more accurate data will require efforts, such as shrinking the aperture size to improve angular resolution, increasing the signal-to-noise ratio of the detector, and reducing reflection from the surrounding environment.

The graphs in Fig. 9(a) and (b) show the correlation of the 3-dB beamwidth and radiant intensity with the number of antennas in the prototype antenna arrays (2 × 2, 4 × 4, 5 × 5, and 6 × 6). The dots represent the measurement results, the dashed line shows the simulation results, and the solid line shows the approximate curve. Fig. 9(a) shows that the 3-dB beamwidth tends to become sharper as the number of antennas increases in both the E-plane and the H-plane, and this is generally consistent with the simulation results. The directivity gain of the 6 × 6 array can be approximately estimated to be 23.9 dB based on

TABLE I
STATE-OF-THE-ART IN RTD-BASED THZ SOURCE

Ref.	This Work	[11]	[12]	[13]	[14]	[15]	[16]
Number of RTDs/antenna	2 RTDs	1 RTD	1 RTD	2 RTDs	1 RTD	1 RTD	2 RTDs
Integrated antenna	Patch	Slot	Slot+Dipole	Slot-Ring	-	CPW+Patch	Patch
Secondary radiator	Unnecessary	Si lens	Unnecessary	Si lens	-	Unnecessary	Unnecessary
Configuration	Array	Array	Array	Single	Single	Single	Single
Number of antennas	36	2	89	1	-	1	1
Coherent oscillation	Coherent	Coherent	Incoherent	-	-	-	-
Oscillation frequency	0.45 THz	0.62 THz	1.00 THz	0.35 THz	0.26 THz	0.69 THz	0.33 THz
Radiation power	11.8 mW	0.61 mW	0.73 mW	0.03 mW	1 mW*	0.01 mW	0.07 mW
3 dB beam width	13°	No data	No data	4°	No data	No data	No data
DC to RF efficiency	1%	No data	No data	No data	0.70%	0.27%	No data

*Data measured by on-wafer probing.

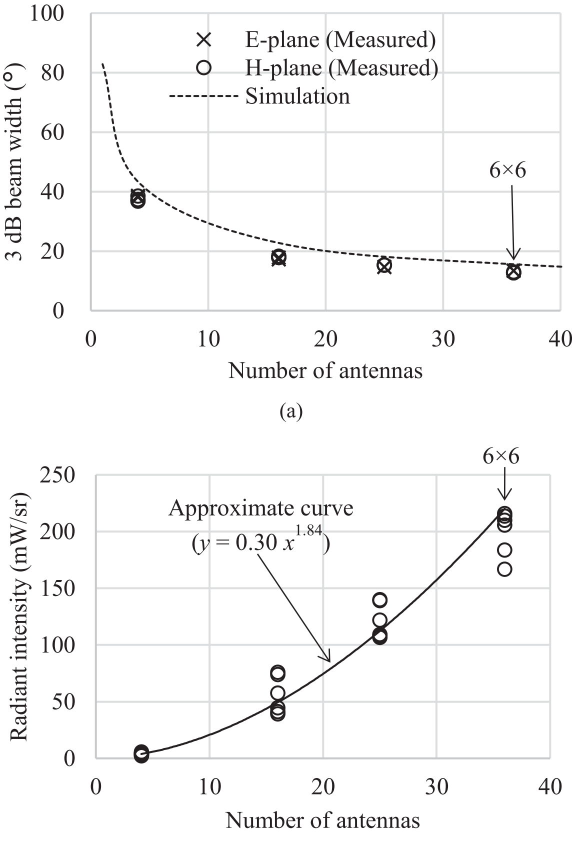

(a)

(b)

Fig. 9. Antenna number dependence of the measured (a) 3-dB beamwidth and (b) radiant intensity.

the measured value of 13° for the 3-dB beamwidth. The radiant intensity is an indicator of the power radiated vertically upward from the antenna, and is calculated by dividing the received power of the bolometer camera in Fig. 7 by the solid angle of 0.0044 sr. According to the graph in Fig. 9(b), the radiant intensity tends to increase with the 1.84th power of the number of antennas, and the measured values for the 6×6 array ranged from 160 to 210 mW/sr. The aforementioned results confirm that an increase in the number of antennas leads to a sharper directivity and stronger radiant intensity, and it is concluded that the proposed active antenna array with integrated patch antenna and RTDs operates with in-phase coherent oscillation. Furthermore, the ability to control the directivity of the device only by adjusting the number of antennas was verified experimentally and analytically; no secondary radiator, such as Si lens or horn antenna, is required.

To bring the correlation between the radiant intensity and the number of antennas close to the ideal square law, it is necessary to reduce the frequency and phase variations of the active antennas at the edge and center of the antenna array of 6×6 to further stabilize injection locking. It is necessary to optimize the design of the coupling line corresponding to an increase in the antenna numbers of 3×3 and over. Detailed studies are required on the lock range of the active antenna array, including the frequency variability of the individual antennas and the strength required for mutual injection locking. Furthermore, by replacing the common feed line with an individual feed line to each antenna, the bias voltage for each antenna can be adjusted, and the frequency can be controlled by the voltage-controlled oscillator, which is an effective method for ensuring a margin against variation [6], [26]. The control of the fabricating variation is also an important issue in the future. Since the relatively high conductor loss in the THz band causes a tradeoff between the number of coupling lines and the output power, it is also important to reduce the transmission loss of the coupling lines connecting the antennas. As a remaining issue for evaluating the performance of this device, it will be necessary to measure the spectral linewidth and antenna gain using a spectrum analyzer for the THz band. We will report on these issues as described earlier at another time.

VI. CONCLUSION

Table I shows state-of-the-art THz sources using RTDs, for comparison with the results [11]–[16]. We propose arraying active antennas with integrated patch antennas and RTDs, as a compact and high-power THz source. Our proposal is a push–pull type active antenna with two RTDs symmetrically integrated in a square patch antenna, and we confirmed that the oscillation frequency in the THz band is tunable with structural adjustments. We developed a prototype of a 6 × 6 active antenna array and obtained a radiation power of 11.8 mW at an oscillation frequency of 0.45 THz. A 6 × 6 array, which was coupled by microstrip lines for mutual injection locking, demonstrated enhanced directivity based on stable in-phase coherent oscillation and rendered a radiant intensity of 210 mW/sr and a 3-dB beamwidth of 13°. Parasitic oscillation in the array antenna was suppressed by a bias stabilization method using *RC* shorts, and the dc to RF efficiency of the 6 × 6 array improved to about 1%. Active antennas with integrated patch antennas and RTDs have the advantage that directivity control is possible by adjusting the number of antennas in the array, even without a secondary radiator. The reported results show that RTDs are promising as practical THz sources for realizing applications of THz imaging and 6G communication.

ACKNOWLEDGMENT

The authors would like to thank T. Saito, T. Yoshioka, T. Itsuji, T. Goden, T. Murao, F. Mizutani, T. Akiyama, K. Ide, and M. Watanabe of Canon, Inc., for their contributions to this work.

REFERENCES

[1] M. Tonouchi, "Cutting-edge terahertz technology," *Nature Photon.*, vol. 1, pp. 97–105, Feb. 2007, doi: 10.1038/nphoton.2007.3.

[2] T. Nagatsuma, "Terahertz technologies: Present and future," *IEICE Electron. Exp.*, vol. 8, no. 14, pp. 1127–1142, Jul. 2011, doi: 10.1587/elex.8.1127.

[3] C. Otani, T. Ikari, and Y. Sasaki, "Development of 300 GHz walk-through body scanner for the security gate applications," in *Proc. SPIE, Terahertz Emitters, Receiv., Appl. XII*, Aug. 2021, vol. 11827, Art. no. 118270N, doi: 10.1117/12.2594528.

[4] G. Valušis, A. Lisauskas, H. Yuan, W. Knap, and H. G. Roskos, "Roadmap of terahertz imaging 2021," *Sensors*, vol. 21, no. 12, Jun. 2021, Art. no. 4092, doi: 10.3390/s21124092.

[5] B. S. Williams, "Terahertz quantum-cascade lasers," *Nature Photon.*, vol. 1, pp. 517–525, Sep. 2007, doi: 10.1038/nphoton.2007.166.

[6] N. Buadana, S. Jameson, and E. Socher, "A multi-port chip scale dielectric resonator antenna for CMOS THz transmitters," *IEEE Trans. Microw. Theory Techn.*, vol. 68, no. 9, pp. 3621–3632, Sep. 2020, doi: 10.1109/TMTT.2020.2993845.

[7] S. Abu-Surra *et al.*, "End-to-end 140 GHz wireless link demonstration with fully-digital beamformed system," in *Proc. IEEE Int. Conf. Commun. Workshops*, Jun. 2021, pp. 1–6, doi: 10.1109/ICCWorkshops50388.2021.9473600.

[8] R. Jain, P. Hillger, E. Ashna, J. Grzyb, and U. R. Pfeiffer, "A 64-pixel 0.42-THz source SoC with spatial modulation diversity for computational imaging," *IEEE J. Solid-State Circuits*, vol. 55, no. 12, pp. 3281–3293, Dec. 2020, doi: 10.1109/JSSC.2020.3018819.

[9] H. Hamada *et al.*, "300-GHz-band 120-Gb/s wireless front-end based on InP-HEMT PAs and mixers," *IEEE J. Solid-State Circuits*, vol. 55, no. 9, pp. 2316–2335, Sep. 2020, doi: 10.1109/JSSC.2020.3005818.

[10] M. Asada and S. Suzuki, "Terahertz emitter using resonant-tunneling diode and applications," *Sensors*, vol. 21, no. 4, Feb. 2021, Art. no. 1384, doi: 10.3390/s21041384.

[11] S. Suzuki, M. Shiraishi, H. Shibayama, and M. Asada, "High-power operation of terahertz oscillators with resonant tunneling diodes using impedance-matched antennas and array configuration," *IEEE J. Sel. Topics Quantum Electron.*, vol. 19, no. 1, Jan./Feb. 2013, Art. no. 8500108, doi: 10.1109/JSTQE.2012.2215017.

[12] K. Kasagi, S. Suzuki, and M. Asada, "Large-scale array of resonant-tunneling diode terahertz oscillator for high output power at 1THz," *J. Appl. Phys.*, vol. 125, Mar. 2019, Art. no. 151601, doi: 10.1063/1.5051007.

[13] S. Iwamatsu, Y. Nishida, M. Fujita, and T. Nagatsuma, "Terahertz coherent oscillator integrated with slot-ring antenna using two resonant tunneling diodes," *Appl. Phys. Exp.*, vol. 14, Jan. 2021, Art. no. 034001, doi: 10.35848/1882-0786/abdb8f.

[14] A. Al-Khalidi *et al.*, "Resonant tunneling diode terahertz sources with up to 1 mW output power in the J-band," *IEEE Trans. Terahertz Sci. Technol.*, vol. 10, no. 2, pp. 150–157, Mar. 2020, doi: 10.1109/TTHZ.2019.2959210.

[15] J. Lee, M. Kim, and J. Lee, "692 GHz high-efficiency compact-size InP-based fundamental RTD oscillator," *IEEE Trans. Terahertz Sci. Technol.*, vol. 11, no. 6, pp. 716–719, Nov. 2021, doi: 10.1109/TTHZ.2021.3108431.

[16] P. Ourednik, T. Hackl, C. Spudat, D. T. Nguyen, and M. Feiginov, "Double-resonant-tunneling-diode patch-antenna oscillators," *Appl. Phys. Lett.*, vol. 119, Dec. 2021, Art. no. 263509, doi: 10.1063/5.0068114.

[17] M. Asada and S. Suzuki, "Theoretical analysis of coupled oscillator array using resonant tunneling diodes in subterahertz and terahertz range," *J. Appl. Phys.*, vol. 103, Jun. 2008, Art. no. 124514, doi: 10.1063/1.2947600.

[18] M. Reddy *et al.*, "Monolithic Schottky-collector resonant tunnel diode oscillator arrays to 650 GHz," *IEEE Electron. Device Lett.*, vol. 18, no. 5, pp. 218–221, May 1997, doi: 10.1109/55.568771.

[19] J. Lin and T. Itoh, "Two-dimensional quasi-optical power-combining arrays using strongly coupled oscillators," *IEEE Trans. Microw. Theory Techn.*, vol. 42, no. 4, pp. 734–741, Apr. 1994, doi: 10.1109/22.285088.

[20] R. Sekiguchi, Y. Koyama, and T. Ouchi, "Subterahertz oscillations from triple-barrier resonant tunneling diodes with integrated patch antennas," *Appl. Phys. Lett.*, vol. 96, Feb. 2010, Art. no. 062115, doi: 10.1063/1.3315868.

[21] Y. Koyama, R. Sekiguchi, and T. Ouchi, "Oscillations up to 1.40 THz from resonant-tunneling diode-based oscillators with integrated patch antennas," *Appl. Phys. Exp.*, vol. 6, May 2013, Art. no. 064102, doi: 10.7567/APEX.6.064102.

[22] R. A. York and R. C. Compton, "Dual-device active patch antenna with improved radiation characteristics," *Electron. Lett.*, vol. 28, pp. 1019–1021, May 1992, doi: 10.1049/el:19920647.

[23] M. Asada, S. Suzuki, and N. Kishimoto, "Resonant tunneling diodes for sub-terahertz and terahertz oscillators," *Jpn. J. Appl. Phys.*, vol. 47, no. 6, pp. 4375–4384, Jun. 2008, doi: 10.1143/JJAP.47.4375.

[24] A. C. Cornescu *et al.*, "High-efficiency bias stabilization for resonant tunneling diode oscillators," *IEEE Trans. Microw. Theory Techn.*, vol. 67, no. 8, pp. 3449–3454, Aug. 2019, doi: 10.1109/TMTT.2019.2916602.

[25] M. Terroux *et al.*, "NEP characterization and analysis method for THz imaging devices," in *Proc. SPIE Passive Act. Millimeter-Wave Imag. XXIV*, 2021, vol. 11745, Art. no. 117450L, doi: 10.1117/12.2586094.

[26] M. Asada, N. Orihashi, and S. Suzuki, "Experiment and theoretical analysis of voltage-controlled sub-THz oscillation of resonant tunneling diodes," *IEICE Trans. Electron.*, vol. 89, no. 7, pp. 965–971, Jul. 2006, doi: 10.1093/ietele/e89-c.7.965.

Yasushi Koyama (Member, IEEE) received the B.E. and M.E. degrees in nuclear engineering from Hokkaido University, Sapporo, Japan, in 1999 and 2001, respectively.

He joined Canon, Inc., Tokyo, Japan, in 2001, where he has been engaged in research and development of solid-state electronic devices with a particular focus on resonant tunneling diode based oscillators for THz imaging applications. He is currently a Lead Engineer with the Semiconductor Device Development Center 1.

Mr. Koyama is a member of the Japan Society of Applied Physics.

Yuki Kitazawa received the B.E. and M.E. degrees in electrical engineering from Hokkaido University, Sapporo, Japan, in 2018 and 2020, respectively.

He joined Canon, Inc., Tokyo, Japan, in 2020, where he has been engaged in research and development of solid-state electronic devices for THz imaging applications. He is currently an Engineer with the Semiconductor Device Development Center 1.

Koji Yukimasa received the B.E. and M.E. degrees in electrical and electronic engineering from the Tokyo Institute of Technology, Tokyo, Japan, in 2005 and 2007, respectively.

He joined Canon, Inc., Tokyo, Japan, in 2007, where he has been engaged in development of wireless communication technology. He is currently an Engineer with the Software Development Center 1.

Tatsuro Uchida received the B.E. and M.E. degrees in functional material science from Saitama University, Saitama, Japan, in 1996 and 1998, respectively.

He joined Canon, Inc., Tokyo, Japan, in 1998, where he has been engaged in research and development of optical devices focus on VCSEL, and process integration technologies of the compound semiconductor and MEMS devices. He is currently a Lead Engineer with the Semiconductor Device Platform Technology Development Center.

Mr. Uchida is a member of the Japan Society of Applied Physics.

Takeshi Yoshioka received the B.E. and M.E. degrees in crystal material engineering from Nagoya University, Nagoya, Japan, in 2009 and 2011, respectively. He joined Canon, Inc., Tokyo, Japan, in 2011, where he has been engaged in research and development of optical devices, and process integration technologies of the compound semiconductor and MEMS devices. He is currently an Engineer with the Semiconductor Device Platform Technology Development Center.

Kokichi Fujimoto received the B.E. and M.E. degrees in applied physics from Tokyo University, Tokyo, Japan, in 2014 and 2016, respectively.

He joined Canon, Inc., Tokyo, Japan, in 2016, where he has been engaged in research and development of optical devices, and process integration technologies of the compound semiconductor and MEMS devices. He is currently an Engineer with the Semiconductor Device Platform Technology Development Center.

Takahiro Sato received the B.E. and M.E. degrees in applied physics from Waseda University, Tokyo, Japan, in 1996 and 1998, respectively.

He joined Canon, Inc., Tokyo, Japan, in 1998, where he has been engaged in research and development of solid-state electronic devices, and display devices. He is currently a Senior Engineer of the Semiconductor Device Platform Technology Development Center.

Jun Iba received the B.E. and M.E. degrees in applied physics from Waseda University, Tokyo, Japan, in 1990 and 1992, respectively.

He joined Canon, Inc., Tokyo, Japan, in 1992, where he has been engaged in research and development of optical technology. He is currently a General Manager for the developments of the compound semiconductor and MEMS devices, with the Semiconductor Device Development Center 1.

Katsuhito Sakurai received the B.S. and M.S. degrees in electrical and communication engineering from Tohoku University, Sendai, Japan, in 1987 and 1989, respectively.

He joined Canon, Inc., Tokyo, Japan, in 1989, where he has been engaged in research and development of integrated circuit and solid-state imaging devices. He is currently a Senior General Manager of the Semiconductor Device Development Center 1.

Takeshi Ichikawa received the B.S. degree in geophysics from Tokyo University, Tokyo, Japan, in 1986.

He joined Canon, Inc., Tokyo, Japan, in 1986, where he has been engaged in research and development of solid-state imaging devices and semiconductor devices. He is currently Executive Officer with Canon, Inc., and Group Executive of the Device Technology Development Headquarters.